

# UCSF

## UC San Francisco Previously Published Works

### Title

Cryo-EM structure of a fungal mitochondrial calcium uniporter

### Permalink

<https://escholarship.org/uc/item/7v291756>

### Journal

Nature, 559(7715)

### ISSN

0028-0836

### Authors

Nguyen, Nam X  
Armache, Jean-Paul  
Lee, Changkeun  
et al.

### Publication Date

2018-07-01

### DOI

10.1038/s41586-018-0333-6

Peer reviewed



Published in final edited form as:

Nature. 2018 July ; 559(7715): 570–574. doi:10.1038/s41586-018-0333-6.

## Cryo-EM structure of the mitochondrial calcium uniporter

Nam X. Nguyen<sup>1,2</sup>, Jean-Paul Armache<sup>3</sup>, Changkeun Lee<sup>1,2,#</sup>, Yi Yang<sup>1,2</sup>, Weizhong Zeng<sup>1,2</sup>, Vamsi K. Mootha<sup>4</sup>, Yifan Cheng<sup>3</sup>, Xiao-chen Bai<sup>2,5,\*</sup>, and Youxing Jiang<sup>1,2,\*</sup>

<sup>1</sup>Howard Hughes Medical Institute and Department of Physiology, University of Texas Southwestern Medical Center, Dallas, Texas, USA

<sup>2</sup>Department of Biophysics, University of Texas Southwestern Medical Center, Dallas, Texas, USA

<sup>3</sup>Howard Hughes Medical Institute and Keck Advanced Microscopy Laboratory, Department of Biochemistry and Biophysics, University of California San Francisco, San Francisco, California, USA

<sup>4</sup>Howard Hughes Medical Institute and Department of Molecular Biology, Massachusetts General Hospital, Harvard Medical School, Broad Institute, Cambridge, Massachusetts, USA

<sup>5</sup>Department of Cell Biology, University of Texas Southwestern Medical Center, Dallas, Texas, USA

### Abstract

The mitochondrial calcium uniporter is a highly selective calcium channel localized to the inner mitochondrial membrane. Here, we describe the structure of an MCU ortholog from the fungus *Neosartorya fischeri* (NfMCU) determined to 3.8 Å resolution by phase-plate cryo-electron microscopy. The channel is a homotetramer with two-fold symmetry in its amino terminal domain (NTD) that adopts a similar structure to that of human MCU. The NTD assembles as a dimer of dimer to form a tetrameric ring that connects to the transmembrane domain through an elongated coiled-coil domain. The ion conducting pore domain maintains four-fold symmetry with the selectivity filter positioned at the start of the pore forming TM2 helix. The aspartate and glutamate sidechains of the conserved DIME motif are oriented toward the central axis and separated by one helical turn. Thus, the structure of NfMCU offers new insights into channel assembly, selective calcium permeation, and inhibitor binding.

---

Users may view, print, copy, and download text and data-mine the content in such documents, for the purposes of academic research, subject always to the full Conditions of use: [http://www.nature.com/authors/editorial\\_policies/license.html#terms](http://www.nature.com/authors/editorial_policies/license.html#terms) Reprints and permissions information is available at [www.nature.com/reprints](http://www.nature.com/reprints).

\*Address correspondence to: Youxing Jiang, Ph.D., Department of Physiology, UT Southwestern Medical Center, 5323 Harry Hines Blvd., Dallas, Texas 75390-9040, Tel. 214 645-6027; Fax. 214 645-6042; [youxing.jiang@utsouthwestern.edu](mailto:youxing.jiang@utsouthwestern.edu). Xiao-chen Bai, Ph.D., Department of Biophysics, UT Southwestern Medical Center, 5323 Harry Hines Blvd., Dallas, Texas 75390-8816, Tel. 214 648-6089; [xiaochen.bai@utsouthwestern.edu](mailto:xiaochen.bai@utsouthwestern.edu).

#Current address: Amgen Discovery Research, Inc. Cambridge, Massachusetts, USA

Correspondence and requests for materials should be addressed to Y.J. ([youxing.jiang@utsouthwestern.edu](mailto:youxing.jiang@utsouthwestern.edu)) or X.B. ([Xiaochen.bai@utsouthwestern.edu](mailto:Xiaochen.bai@utsouthwestern.edu)).

### Author contributions

N.X.N., V.K.M. and Y.J. conceived the study. N.X.N., J-P.A., Y.J., Y.C. and X.B. designed the experiments and analyzed the data. N.X.N., J-P.A., C.L., Y.Y., W.Z., and X.B. generated key materials and executed the experiments. N.X.N. and Y.J. wrote the manuscript with input from J-P.A., Y.C., V.K.M. and X.B. Y.J. supervised the project and revised the manuscript.

The authors declare no competing financial interests.

## Introduction

Mitochondria can take up large amounts of calcium from their environment, which can modulate ATP production, alter cytoplasmic  $\text{Ca}^{2+}$  dynamics, and trigger cell death<sup>1,2</sup>. Calcium enters the mitochondria matrix through the mitochondrial calcium uniporter, a highly selective calcium channel that is localized to the inner mitochondrial membrane<sup>3</sup>. In humans, the uniporter is a protein complex, or “uniplex”, consisting of at least four components: the ion conducting pore – MCU<sup>4,5</sup>, an essential membrane spanning subunit – EMRE<sup>6</sup>, and peripheral membrane gate-keeping proteins – MICU1 and MICU2<sup>7,8</sup>. While MCU is found in all major eukaryotic taxa, EMRE is metazoan-specific and is required for the conductivity of MCU in these organisms<sup>6,9</sup>. On the contrary, the *Dictyostelium* MCU homolog, whose genome lacks EMRE, is sufficient to operate as a pore-forming channel<sup>10</sup>. Uniporter activity has diverged in fungi, even being lost entirely in certain lineages such as *S. cerevisiae*<sup>11</sup>. In most fungi, the pore-forming MCU is the only component of the uniporter based on genome sequence analysis<sup>12</sup> and likely represents the minimal channel component of the uniporter for calcium uptake. A recent study utilized functional mutagenesis to demonstrate that the MCU ortholog from the fungus *Aspergillus fumigatus* can mediate  $\text{Ca}^{2+}$  transport into mitochondria<sup>13</sup>.

Interestingly, MCU exhibits no discernible sequence homology to other cation channels<sup>12</sup>, making it difficult to predict structure and function using computational tools. Although the structures of various isolated MCU domains or the auxiliary component of the uniplex have been reported – the N-terminal domain (NTD) of human MCU<sup>14,15</sup>, the pore domain of an N-terminal deletion of the *C. elegans* MCU or cMCU-NTD<sup>16</sup>, and human MICU1<sup>17</sup> – fundamental questions about the channel’s assembly, gating, and ion permeation remain unanswered. The recent NMR structure of the cMCU-NTD revealed a pentameric channel pore with an occluded ion pathway and EMRE was suggested to be the key to driving the pore from being in the occluded to an open, ion conductive state<sup>16</sup>; however, there is no structural data on metazoan MCU and EMRE together. Mounting evidence for the pathophysiological relevance of the uniporter complex<sup>1,18</sup> provides further impetus for structure determination of the intact channel. To address these longstanding questions, we determined the cryo-EM structure of an MCU homolog from *Neosartorya fischeri*, NfMCU, and also performed in-depth functional studies on this uncharacterized channel. The structure defines the architecture of the channel subunit of the MCU and sheds insights into channel assembly and function.

## Biochemistry and structure determination

The architectural and functional complexity of metazoan MCU led us to take a reductionist approach and characterized MCU orthologs from fungi, whose genomes encode for only the ion conducting pore subunit<sup>12</sup>, with the goal of understanding basic principles governing channel assembly and function. Among those tested, the 488-residue wildtype MCU ortholog from *Neosartorya fischeri*, NfMCU, showed the best biochemical properties in terms of protein expression and stability and was modified for structural studies (see Methods). Unlike the pentameric cMCU-NTD from the NMR study<sup>16</sup>, NfMCU purified as a tetramer in solution (Extended Data Fig. 1). Additionally, it confers uniporter function to

bacteria and NfMCU proteoliposomes recapitulate the voltage-dependent  $\text{Ca}^{2+}$  uptake property of the MCU<sup>19</sup> (Methods and Extended Data Fig. 2).

Structure determination of NfMCU using single particle cryo-EM was technically challenging for the following reasons: small protein size of 180kDa for a channel tetramer, symmetry mismatch between the pore and soluble domains, and an elongated shape with minimal features. Also, detergent solubilized NfMCU aggregated when frozen and those in amphipols exhibited orientation bias. We first overcame the stability issue by reconstituting the channel into nanodiscs but, owing to the channel's flexibility in nanodiscs, whose size is much larger than the transmembrane part of the channel, we could only determine the structure to ~15 Å resolution. This led us to consider using the newly developed scaffolding protein saposin for reconstitution (see Methods)<sup>20</sup>, which we rationalized could adapt its oligomerization to maintain NfMCU in an artificial lipid bilayer that is proportional to the channel's smaller transmembrane domain. NfMCU reconstituted in saposin markedly improved the structure to an overall resolution of 4.6 Å; however, several parts of the channel were poorly resolved, likely due to inaccurate particle alignment stemming from the inherently low contrast of small particles. Finally, we used a Volta phase plate to image the NfMCU saposin complex, which ultimately allowed us to determine the structure to an overall resolution of 3.8 Å according to the gold-standard Fourier shell correlation 0.143 criterion (Extended Data Fig. 3, Extended Data Table 1 and Methods).

Consistent with our biochemical analysis of NfMCU in detergent, the EM map unambiguously shows tetrameric assembly of NfMCU (Fig. 1a). The map was of sufficient quality for model building of major parts of the protein (Extended Data Fig. 4 and Methods). However, parts of the N- and C-termini as well as the long loop in the NTD were disordered and were not modeled in the final structure (Methods). The EM map also revealed clear electron density for the 81-residue saposin, which we modeled as poly-alanine (Extended Data Fig. 5). Six saposin molecules – each forming a C-shaped clamp oriented at a ~45° angle to the central axis – encircle the lipid bilayer to stabilize NfMCU. Thus, for the first time, our structure also reveals how saposin oligomerizes to maintain a membrane protein in lipid.

## Overall architecture of NfMCU

NfMCU forms an elongated, three-tiered channel tetramer with each tier corresponding to a structural domain: the N-terminal domain (NTD), coiled coil domain (CCD) and transmembrane domain (TMD) (Fig. 1b and Extended Data Fig. 6). Although NfMCU is tetrameric, it transitions from being four-fold symmetric at the TMD to two-fold symmetric in the NTD, which forms a dimer of dimer (Fig. 1c, 2a). Unlike the NMR structure of cMCU-NTD, which lacks the NTD and adopts a constricted architecture, NfMCU is architecturally open, with large fenestrations in the space defined by the CCD (Fig. 1b and Extended Data Fig. 7a). Sitting atop the NTD, the CCD resembles pillars supporting the TMD. The tight packing among the four NTD subunits, as well as the exceptionally long CC1 helix that extends into TM1, dictates the spacing among the four CCDs, thereby, creating a highly solvent accessible space below the ion conduction pathway.

There are several major differences between the structure of NfMCU and cMCU-NTD (Extended Data Fig. 7a, b). In addition to their oligomeric states and overall architecture, the secondary structural elements between the two structures are also quite different. The CC1 and TM1 is a single extended helix in NfMCU but is five short, broken helices in cMCU-NTD (Extended Data Fig. 7b). These structural differences are unlikely to be caused by the different origins of the two channels, as the CCD, TMD and selectivity filter are highly conserved among MCU orthologs<sup>12</sup> (Extended Data Fig. 6). We suspect that the missing NTD and the use of a denaturing detergent like fos-choline to extract and purify protein from inclusion bodies in the NMR study contributed to the discrepancy.

## Luminal soluble domains

The NTD and CCD constitute the luminal soluble domains of NfMCU. Despite the poor sequence conservation of the NTD among MCU orthologs<sup>12</sup> (Extended Data Fig. 6), the structures of the NTDs from NfMCU and human MCU are strikingly similar<sup>14,15</sup>. Consisting of seven beta stands ( $\beta$ 1-7) and two helices ( $\alpha$ 1 and 2), each NTD forms a barrel enclosed by the 7-stranded  $\beta$  sheet and the  $\alpha$ 1 helix with the  $\alpha$ 2 helix sitting atop the barrel (Extended Data Fig. 7b). Four NTDs form a well-packed tetrameric ring in a dimer of dimer configuration with two-fold symmetry (Fig. 2a). Inter-subunit interactions are defined by two types of interfaces. Interface I involves primarily hydrogen bonding between main chain atoms on  $\beta$ 5 of one subunit and  $\beta$ 3 of a neighboring subunit (Fig. 2b) while interface II is stabilized by hydrogen bonding between polar side chains (Fig. 2c). A similar dimerization at interface I is also observed in the crystal structure of HsMCU<sub>NTD</sub> (Extended Data Fig. 7c), thus highlighting the structural conservation of NfMCU to human MCU. The tetrameric assembly of the NTD implies its role in maintaining the channel's architectural integrity. However, its functional importance is not entirely clear based on studies of human MCU<sup>14,16</sup> and, thus, warrants further studies.

The CCD consists of four helices labeled as CC1,  $\alpha$ 3, CC2 and  $\alpha$ 4 (Fig. 1d and Extended Data Fig. 6). The first coiled-coil (CC1) forms an exceptionally long alpha helix that curves with respect to the central axis as it extends from the NTD toward the TMD – transitioning seamlessly into TM1. A juxtamembrane loop (JML) – approximately 10 residues – and the  $\alpha$ 3 helix connect the end of TM2 to the second coiled-coil (CC2) in two distinct conformations between two neighboring subunits (Fig. 1d). In one subunit, the loop runs parallel to the membrane and the  $\alpha$ 3 helix runs almost parallel to CC1, while in the other subunit the loop extends nearly perpendicularly from the membrane and the  $\alpha$ 3 helix becomes more perpendicular to CC1. The CC2 helix runs nearly parallel to CC1 to form a coiled-coil and the CCD ends with the short  $\alpha$ 4 helix that runs perpendicularly to the coiled-coil, jutting away from the central axis (Fig. 1d).

## Ion-conducting pore

The NfMCU pore is architecturally unique as compared to classical 2-TM tetrameric cation channels like KcsA<sup>21</sup>, whose outer TM1 helix wraps around the inner pore forming TM2 helix, generating an inverted teepee-shaped ion conduction pore. Pillared by four TM1s, the transmembrane helices of NfMCU enclose a cone-shaped ion conduction pore with wider

opening at the luminal side (Fig. 3 and 4a). Interestingly, the pore forming TM2 makes very little contact with the TM1 from the same subunit but rather extensively with a neighboring TM1 (Fig. 3a). Consequently, there is a wide gap between TM1 and TM2 within each subunit at the luminal half of the membrane, which we expect to be sealed by lipid.

NfMCU also lacks the canonical re-entrant pore loop and helix that defines the selectivity filter of tetrameric cation channels; instead, the filter residues constitute the first helical turn of TM2. The conserved acidic residues of the DIME motif, which is  ${}_{369}\text{DTME}_{372}$  in NfMCU, point toward the central axis and are separated by about one helical turn (Fig. 4). Four D369 residues encircle the cytosolic pore entrance of NfMCU with a diagonal distance of  $\sim 8.0$  Å between carboxylate oxygen atoms. The side chains of E372 form the narrowest part of the filter with the narrowest opposing carboxylate oxygens measuring about 4.5 Å (Fig. 4b). As NfMCU was maintained in 1mM  $\text{CaCl}_2$  throughout sample preparation, we also observed a strong electron density at the center of the E372 ring, which we assigned as a  $\text{Ca}^{2+}$  chelated by two opposing E372s in a bidentate manner with ion-ligand distances between 2.2 – 2.5 Å, optimal for  $\text{Ca}^{2+}$  coordination (Fig. 4c, d). The protein packing around the filter region also provides insights into the evolutionary conservation of several residues within the proximity of the DIME motif. W368 intercalates between TM2 of each subunit with its indole ring oriented nearly vertically; its phenyl ring forms  $\text{CH}/\pi$  interactions with the highly conserved P373 in a stacked-like configuration<sup>22,23</sup> while the amino group of the pyrrole ring forms intra- and intermolecular hydrogen bonds with the carboxylate oxygen of E372 (Fig. 4c, d). Replacing W368 or P373 with alanine resulted in non-functional channels (Fig. 4e). Thus, the region constituting the selectivity filter of NfMCU is tightly packed and conformationally rigid.

Beyond the selectivity filter, the pore opens into a large, mainly hydrophobic cavity that widens toward the base of the ion conduction pathway rather than constrict as seen among canonical tetrameric cation channels (Fig. 4a). Whether gating occurs within the ion conducting pore is unclear and warrants further studies. However, our *in vitro*  ${}^{45}\text{Ca}^{2+}$  flux assay and bacteria  $\text{Ca}^{2+}$  uptake assay seem to suggest that NfMCU functions as a constitutively open channel since the only conditions required to stimulate  $\text{Ca}^{2+}$  uptake is an electrochemical gradient. Our speculation is also supported by the general consensus that  $\text{Ca}^{2+}$  activation of the human uniporter is mediated by MICU1 and MICU2 rather the channel itself<sup>24-27</sup>.

## **$\text{Ca}^{2+}$ permeation and inhibitor binding**

The proximity of the two rings of acidic residues – D369s and E372s – within the selectivity filter of NfMCU suggests a two-site, single file pore for selective  $\text{Ca}^{2+}$  permeation in MCU, which is conceptually similar to the classical ion conduction model for voltage-gated  $\text{Ca}^{2+}$  channel ( $\text{Ca}_v$ )<sup>28,29</sup>. With a larger diameter, the ring of D369s at the cytosolic entrance encircles a low affinity  $\text{Ca}^{2+}$  site (site 1) for hydrated ion. The site is likely non-specific, but preferable for  $\text{Ca}^{2+}$  given the highly negative charge of the ring. The narrow ring consisting of E372s forms the high affinity,  $\text{Ca}^{2+}$  selective site (site 2) with the acidic side chains directly chelating  $\text{Ca}^{2+}$ , analogous to the high affinity  $\text{Ca}^{2+}$  site formed by the EEEE locus of  $\text{Ca}_v$  channels<sup>30</sup>. Also, the structural constraint of E372 forces the carboxylate side chains

to be near each other – making an empty site 2 energetically unfavorable due to electrostatic repulsion. To mitigate this effect, we suspect that site 2 is constitutively bound to  $\text{Ca}^{2+}$  with high affinity, which can be accomplished at physiological condition given that MCU has high affinity for  $\text{Ca}^{2+}$  ( $\sim 2\text{nM}$ )<sup>3</sup>. Thus, a potential mechanism for  $\text{Ca}^{2+}$  transport in MCU likely follows a similar model proposed for  $\text{Ca}_V$  channels (Fig. 5a):  $\text{Ca}^{2+}$  constitutively binds to site 2 under physiological condition and blocks the permeation of  $\text{Na}^+$  or  $\text{K}^+$ . With increasing cytosolic  $\text{Ca}^{2+}$  concentration,  $\text{Ca}^{2+}$  gradually occupies site 1 and, thereby, provide the necessary electrostatic repulsion between sites 1 and 2 to lower the affinity of the site 2  $\text{Ca}^{2+}$ , allowing it to be readily knocked off and move into the water filled vestibule directly below the filter. This  $\text{Ca}^{2+}$  permeation cycle repeats as the  $\text{Ca}^{2+}$  from site 1 hops to site 2 freeing site 1 to bind a new  $\text{Ca}^{2+}$ . The presence of the low affinity site external to the high affinity site may also explain the inward rectification of  $\text{Ca}^{2+}$  permeation observed in MCU.

The two-site model implies that the high affinity site 2 is essential for  $\text{Ca}^{2+}$  selectivity while the low affinity site 1 is less specific but necessary for efficient  $\text{Ca}^{2+}$  permeation. The roles of the acidic residues at both sites for  $\text{Ca}^{2+}$  permeation were tested in NfMCU using our bacteria uptake assay. We first examined the effect of neutralizing the two acidic residues individually (D369N and E372Q). Consistent with observations in human MCU<sup>4,16</sup>, the E372Q mutant no longer conducts  $\text{Ca}^{2+}$  while the D369N mutant exhibited a slight reduction in  $\text{Ca}^{2+}$  uptake (Fig. 5b and Extended Data Fig. 8). We also asked whether disrupting the ion coordination distance had any effect on channel function. Interestingly, a D369E mutation showed  $\sim 50\%$  greater  $\text{Ca}^{2+}$  uptake rate compared to the WT while the E372D mutant remained nonfunctional. A similar D261E mutation in human MCU – the equivalent mutation as D369E for NfMCU – showed a slight reduction in calcium uptake<sup>16</sup>. Mutating D369 to threonine or glutamine yielded nonfunctional channels. These data confirm that site 2 (E372), which is essential for specific  $\text{Ca}^{2+}$  binding, is highly sensitive to mutations whereas the non-specific site 1 (D369) is more tolerable to mutations.

The structure of NfMCU also offers a unique opportunity to probe the mechanism of Ru360 binding. In human MCU, a serine (S259) two residues preceding the DIME motif was initially identified to be important for Ru360 binding<sup>4</sup>, since an alanine mutant conferred resistance to the drug while still allowing calcium transport. In NfMCU, the equivalent residue is a glycine. Studies on cMCU-NTD identified the aspartate of the DIME motif as a second key residue for Ru360 binding<sup>31</sup>, which we suspect is the primary Ru360 binding site for NfMCU since the DIME motif is conserved across all MCU orthologs. Neutralizing the aspartate (D369N) weakened Ru360 blocking while maintaining the charge but reducing the pore diameter at site 1 (D369E) eliminated Ru360 blocking (Fig. 5c, d). This result confirms that D369 in NfMCU forms the primary blocking site for Ru360, whose binding is dictated by the charge as well as the pore size at site 1.

## Conclusion

Thus, the structure of NfMCU provides the first model of an intact mitochondrial calcium uniporter determined to near atomic resolution, shedding new insights into channel assembly and function. Contrary to the structure of cMCU-NTD, NfMCU functions as a tetrameric calcium channel, whose pore is poised for rapid ion conduction. In essence, the channel

provides a rather finite barrier measuring  $\sim 6 \text{ \AA}$  – the distance separating the filter aspartate and glutamate – that  $\text{Ca}^{2+}$  must traverse from the intermembrane space to the matrix. The combination of having two ion binding sites and a huge electrochemical gradient across the inner mitochondrial membrane provide the necessary driving force for MCU to selectively conduct  $\text{Ca}^{2+}$ . It is notable that early studies of calcium transport demonstrated that mitochondria from diverse eukaryotes have uniporter activity<sup>11</sup>. However, the kinetics and apparent binding affinities of calcium uptake by fungal mitochondria are appreciably different from that of vertebrate<sup>11</sup>. While NfMCU reveals the architectural arrangement of the basic channel component of the uniporter, further study is needed to address some fundamental questions about metazoan uniporter function, such as how metazoan MCU evolved to require EMRE for ion conduction and how MICU1 and MICU2 confer  $\text{Ca}^{2+}$ -dependent gating to the uniplex.

## Methods

### Expression and purification of NfMCU

The construct for NfMCU (NCBI accession number: XP\_001266985.1), which was codon optimized for expression in *E. coli* and cloned into the pCOLD II vector<sup>32</sup>. For functional assay, the full-length protein with only the mitochondrial targeting sequence removed (see Extended Data Fig. 5) was modified to contain an N-terminal 6x-His tag and a thrombin cleavage site (LVPRGS) and then reinserted back into the pCOLD II vector (Takara) using the restriction sites NdeI/XhoI. For structural studies, the NfMCU construct used in the function assay was further truncated by an additional 10 residues each from the N- and C-termini and then cloned into the pCOLD II vector using the same restriction sites. Although no significant functional difference was observed between the full-length protein and the truncated channel (Extended Data Fig. 1b), the truncated construct yields a significantly more monodispersed profile on gel filtration and was subsequently used for structural studies (Extended Data Fig. 1a). All single-site mutants were generated using the Quikchange Site-Directed Mutagenesis Kit (Agilent) and confirmed by DNA sequencing.

*E. coli* (BL21 DE3) were freshly transformed, plated onto LB/ampicillin (LB/Amp) agar, and grown overnight. Colonies were harvested directly from LB/Amp plates to seed LB media (100 $\mu\text{g}/\text{mL}$  ampicillin) and grown in shaker flasks at 37°C in an orbital shaker until the cells reached an  $\text{OD}_{600} = 0.37\text{--}0.4$ , at which point they were transferred to another orbital shaker pre-chilled to 15°C and allowed to grow for another hour before protein expression was induced by addition of IPTG to a final concentration of 0.4mM. Cells were then grown at 15°C for 16–18 hours before being harvested. The cell pellets were flash frozen in liquid nitrogen and stored at  $-80^\circ\text{C}$ .

To purify NfMCU, the cell pellets were resuspended in lysis buffer (50mM Tris pH 8, 300mM NaCl, 1mM  $\text{CaCl}_2$ ), supplemented with protease inhibitors (1  $\mu\text{g}/\text{mL}$  each of DNase I, pepstatin, leupeptin and aprotinin, and 1 mM PMSF), and then homogenized on ice. To remove inclusion bodies and misfolded protein, the homogenate was centrifuged at 10,000  $\times$  g for 20 minutes at 4°C. The supernatant was harvested and NfMCU was extracted with 1% (w:v) n-dodecyl- $\beta$ -D-maltopyranoside (DDM, Anatrace) by gentle agitation for 1 hour on ice. After extraction, the supernatant was collected following a 30-minute centrifugation at



21,000 × g at 4°C and then incubated with Ni-NTA resin (Qiagen) with gentle agitation on ice for 1 hour. The resin was collected on a disposable gravity column (Bio-Rad), washed with wash buffer A (lysis buffer + 1mM DDM) for 3 column volumes and then with wash buffer B (lysis buffer + 1mM DDM + 30mM imidazole) for 10 column volumes. NfMCU was eluted with wash buffer C (lysis buffer + 1mM DDM + 300 mM imidazole). Thrombin was added at a ratio of 1 unit of thrombin per 1L culture of bacterial cell pellet; the sample was allowed to incubate at 20°C, overnight, to remove the His-tag. NfMCU is then concentrated and further purified by size exclusion chromatography on a Superdex 200 10/300 GL column (GE Healthcare) pre-equilibrated with buffer D (20mM HEPES pH 7.5, 300mM NaCl, 1mM CaCl<sub>2</sub>, 1mM DDM). The main peak (eluting around 11mL) was then collected for further biochemical and structural analysis.

### Reconstitution of NfMCU into saposin

We were unsuccessful in reconstituting NfMCU following the original protocol<sup>20</sup>, likely due to the recommended step of heat shocking the sample during reconstitution. We thus made some modifications to the protocol, which we believe is better suited for more sensitive or less stable membrane proteins. Our reaction consists of the following components mixed at a molar ratio of 1:3:10 (NfMCU : saposin : *E. coli* total lipids). As a substitution for the recommended heat-shock step<sup>20</sup>, saposin was destabilized by incubation with sodium cholate (15mM final concentration) with rotation at 4 °C for 1 hour. Purified NfMCU (concentrated to 100µM) was then added to the reaction and allowed to rotate at 4°C for 1 hour before addition of BioBeads (BioRad) to remove detergents. The reaction was incubated with BioBeads for 3–4 hours at 4°C, and BioBeads exchange was performed a total of 3 times with each incubation step lasting 3–4 hours at 4°C. The reconstituted NfMCU saposin complex was separated from empty saposin complex and aggregates by gel filtration chromatography on a Superdex 200 10/300 GL column (GE Healthcare) pre-equilibrated with buffer E (20mM HEPES pH 7.5, 300mM NaCl, 1mM CaCl<sub>2</sub>, 2% glycerol). The main peak (eluting around 11mL) was then collected for structural analysis.

### EM data acquisition

Prior to freezing grids, the NfMCU saposin complex (concentrated to 0.6mg/mL) was incubated with 50µM Ru360 on ice for 30 minutes. The cryo-EM grids were prepared by applying 3 µL of the NfMCU-saposin-Ru360 complex to a glow-discharged Quantifoil R1.2/1.3 300-mesh gold holey carbon grid (Quantifoil, Micro Tools GmbH, Germany) and blotted for 4.0 seconds under 100% humidity at 4 °C before being plunged into liquid ethane using a Mark IV Vitrobot (FEI). Micrographs were acquired on a Titan Krios microscope (FEI) operated at 300 kV with a K2 Summit direct electron detector (Gatan), using a slit width of 20 eV on a GIF-Quantum energy filter as well as a Volta phase plate following the same approach for phase plate data collection as previously described<sup>33</sup>. EPU software (FEI) was used for automated data collection following standard FEI procedure. A calibrated magnification of 59,523X was used for imaging, yielding a pixel size of 0.84 Å on images. The defocus was set at -0.5 µm. Each micrograph was dose-fractionated to 30 frames under a dose rate of 4 e<sup>-</sup>/pixel/s, with a total exposure time of 12 s, resulting in a total dose of about 60 e<sup>-</sup>/Å<sup>2</sup>.

## Image processing

For the NfMCU phase plate dataset, motion correction was performed using the MotionCorr2 program<sup>34</sup>, and the CTF parameters of the micrographs were estimated using the GCTF program<sup>35</sup>. All other steps of image processing were performed using RELION<sup>36</sup>. Initially, about 1,000 particles were manually picked from a few micrographs. Class averages representing projections of NfMCU in different orientations were selected from the 2D classification of the manually picked particles, and used as templates for automated particle picking from the full data set of 2,470 micrographs. The 526,554 extracted particles were binned 3 times and subjected to two rounds of 2D classification, and a total of 355,929 particles were finally selected for 3D classification using the initial model generated by RELION as the reference. Two of the 3D classes showed good secondary structural features and their particles were selected, combined and re-extracted into the original pixel size of 0.84 Å. After 3D refinement with *C*<sub>2</sub> symmetry imposed and particle polishing, the resulting 3D reconstructions from 128,231 particles yielded an EM-map with a resolution of 3.8 Å. The transmembrane domain showed poor density, indicating a local structural heterogeneity. Therefore, we performed a focused 3D classification with density subtraction in order to improve the density of the transmembrane domain<sup>37</sup>. In this approach, the density corresponding to the soluble domains of the channel as well as the belt-like density from saposin was subtracted from the original particles. The subsequent 3D classification on the modified particles was carried out by applying a mask around the transmembrane domain and having all the orientations fixed at the value determined in the initial 3D refinement. After this round of classification, one class (83,343 particles) with better density in the transmembrane domain was selected for 3D refinement, yielding an EM map of 3.8 Å in which the entire transmembrane domain can be modeled. All resolutions were estimated by applying a soft mask around the protein density and the gold-standard Fourier shell correlation (FSC) = 0.143 criterion. ResMap<sup>38</sup> was used to calculate the local resolution map.

## Model building, refinement, and validation

*De novo* atomic model building was conducted in Coot<sup>39</sup>. Since the crystal structure of the NTD of human MCU<sup>14</sup> (PDB: 4XTB) fits nicely in the EM map, it was used as a guide to build the NTD of NfMCU. Amino acid assignment was achieved based on the clearly defined density for bulky residues (Phe, Trp, Tyr, and Arg). Models were refined against summed maps using phenix.real\_space\_refine<sup>40</sup>, with secondary structure restraints applied. The model was validated using previously described methods to avoid overfitting<sup>41,42</sup>. The 3.8 Å EM density map of NfMCU allowed us to construct a model containing the following residues: chain A, B: 124–200, 258–399, and 406–461; chain C, D: 124–196, 259–396, and 404–461. Although we added Ru360 in our sample with the hope of seeing how it blocks the channel pore, its density was not visible in the structure. One main reason could be the symmetry mismatch. As the MCU pore entrance has 4-fold symmetry, Ru360 could bind to the pore in four different orientations, causing its density to be averaged out. The statistics for the model's geometries were generated using MolProbity<sup>43</sup>. Pore radii were calculated using the HOLE program<sup>44</sup>. All the figures were prepared in PyMol<sup>45</sup> or Chimera<sup>46</sup>.

## Bacterial calcium uptake assay

*E. coli* expressing NfMCU were grown as described above with the exception that protein induction was allowed to proceed for 16 hours, at which time the cells were harvested, centrifuged at  $4000 \times g$  for 10 minutes at  $4^{\circ}\text{C}$ , and the media was discarded. To remove residual media, the cell pellet was resuspended in ice-cold buffer (50mM HEPES pH 7.4, 150mM KCl) and then centrifuged again ( $4000 \times g$  for 10 minutes at  $4^{\circ}\text{C}$ ) and the supernatant was discarded. To prepare the bacteria for calcium uptake measurements, the bacteria were treated as though they were mitochondria and prepared as previously described for the purification of mitochondria from yeast<sup>47</sup> but with slight modifications. To remove residual  $\text{Ca}^{2+}$ , the cells were resuspended to a final concentration of 10mg/mL in ice-cold bacteria prep buffer (0.6M D-mannitol, 10mM  $\text{KH}_2\text{PO}_4$ , 20mM HEPES pH 7.4, 5mg/mL bovine serum albumin) plus 1mM EDTA and allowed to shake gently on ice for 30 minutes. To replenish any  $\text{Mg}^{2+}$  that was chelated by EDTA treatment, 2mM  $\text{MgCl}_2$  was then added into the cell resuspension followed by gentle shaking on ice for another 30 minutes. The cells were then centrifuged ( $4000 \times g$  for 10 minutes at  $4^{\circ}\text{C}$ ) and the supernatant was discarded. The cells were centrifuged again ( $4000 \times g$  for 3 minutes at  $4^{\circ}\text{C}$ ) and residual buffer was removed with a pipette. The wet weight of the bacteria was measured with a digital balance (typical yield is  $\sim 80\text{mg}$  of bacteria per 30mL culture of bacteria). The cells were then resuspended in ice-cold reaction buffer (0.6M D-mannitol, 20mM HEPES pH 6.8,  $10\mu\text{M}$  EGTA, 0.5mg/mL bovine serum albumin) to a final concentration of 10mg/mL and were used immediately for calcium uptake measurement.

To measure calcium uptake, we relied on the highly negative membrane potential across the plasma membrane of *E. coli*<sup>48</sup> and used the fluorescent calcium indicator Oregon Green BAPTA-6F (Life Technologies), which was added to a final concentration of  $1\mu\text{M}$  (from aliquots of a  $500\mu\text{M}$  stock kept at  $-20^{\circ}\text{C}$ ) to cells resuspended in reaction buffer, to monitor the  $\text{Ca}^{2+}$  concentration changes over time using fluorescence signal – a conventional approach for monitoring mitochondrial calcium uptake in the field<sup>4,5</sup>. For calcium uptake measurements,  $100\mu\text{L}$  of cell suspension was added to a 96-well plate (Corning) and fluorescence was monitored in a Molecular Devices SpectraMax M3 plate reader (excitation/emission: 485nm/535nm). Baseline fluorescence was measured for all samples at the start of each reaction for 60 seconds followed by addition of  $5\mu\text{L}$   $\text{CaCl}_2$  stock to the  $100\mu\text{L}$  reaction in any experiment to reach the desired concentration. With the exception of the experiment in Figure 1A, where the bacteria were pulsed 3 times with  $20\mu\text{M}$   $\text{CaCl}_2$ , all measurements were from samples pulsed only once with the concentration of  $\text{CaCl}_2$  indicated in the figure legend. Fluorescence was monitored for 4 minutes to assess calcium uptake.

For the inhibition experiments (either with  $\text{GdCl}_3$  or Ru360), the inhibitor was added to  $1000\mu\text{L}$  of cell suspension to the highest desired concentration of inhibitor for the experiment and this cell suspension was then used as a stock to dilute into a cell suspension without any inhibitor added (to a final volume of  $100\mu\text{L}$ ) to obtain a series of cells in the desired inhibitor concentration. The samples were then pulsed with  $50\mu\text{M}$   $\text{CaCl}_2$  and fluorescence was monitored for 4 minutes.

To ensure protein expression was comparable among the NfMCU mutants tested in our uptake assay, Western blot analysis was performed on each sample used for each

experiment. Extended Data Figure 8 shows representative Western blots of an experimental trial using the NfMCU mutants referred to in this study. Mouse anti-His antibodies (Qiagen) was used to detect NfMCU expression and mouse anti-E. coli RNA polymerase alpha or anti-RpoA (Santa Cruz Biotechnology) was used as a loading control. HRP-conjugated sheep anti-mouse antibodies were used as the secondary antibodies (GE Healthcare).

All data were analyzed in GraphPad Prism 7 (GraphPad Software, Inc.). To obtain the rate of calcium uptake, the linear phase of the uptake measurement – the first 45–60 seconds of the reaction following  $\text{CaCl}_2$  administration – was determined by fitting the data to a linear regression equation in GraphPad Prism; the slope of the fit is taken as the rate of calcium uptake. Further analysis such as normalization are indicated in the figure legend. To obtain the  $\text{IC}_{50}$  for Ru360, the relative calcium uptake rates were fitted to a dose-response curve in GraphPad Prism.

### Radioactive $^{45}\text{Ca}$ flux assay

In light of the contradiction of the oligomeric state between NfMCU and cMCU-NTD, we designed an *in vitro* functional assay by reconstituting our purified tetrameric channel into liposomes. Unable to obtain currents of NfMCU by electrophysiology – probably due to the channel's small conductance – we performed a radioactive  $^{45}\text{Ca}$  flux assay on proteoliposomes loaded with 150mM KCl.

NfMCU was reconstituted into lipid vesicles using a similar protocol as described<sup>49</sup>. *E. coli* total lipid (Avanti) was prepared following standard protocol and then solubilized in dialysis buffer (50mM HEPES pH 7.4, 150mM KCl) supplemented with 40mM n-decyl- $\beta$ -D-maltopyranoside (DM, Anatrace). Purified NfMCU in DDM (at ~1mg/mL) was mixed with the DM-solubilized *E. coli* total lipid at a ratio of 1:100 (w:w, protein:lipids). NfMCU and lipid mixture were incubated with gentle rotation at 4°C for 1 hour and then dialyzed (using dialysis tubing with a molecular weight cutoff of 12,000–14,000 Da, Spectra/Por) against 1L of dialysis buffer at 4°C to remove detergent. Fresh dialysis buffer (1L each time) was exchanged every 18–20 hours for a total of 3 exchanges. Following dialysis, NfMCU proteoliposomes were divided into 100 $\mu\text{L}$  aliquots, flash frozen in liquid nitrogen, and stored at –80°C. For all flux assays, three separate batches of bacteria were grown to express NfMCU. The protein was then purified individually and used immediately for reconstitution into liposomes.

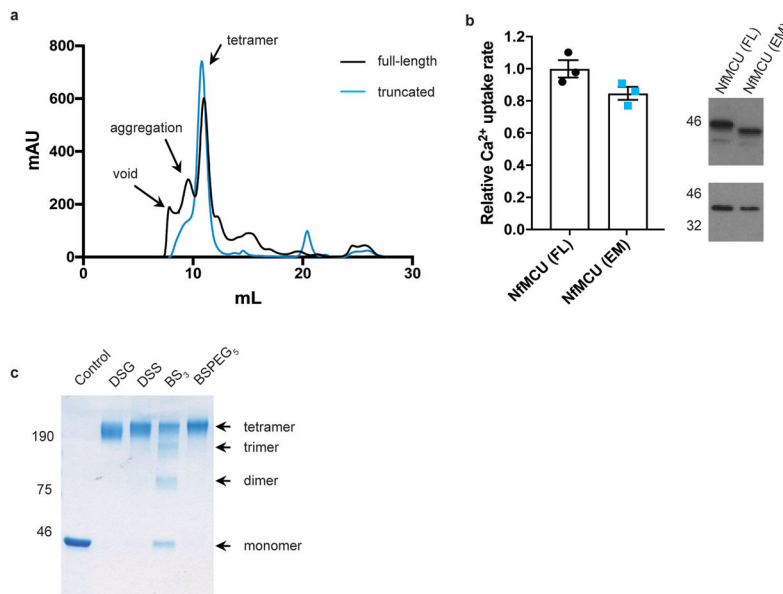
The  $^{45}\text{Ca}$  flux assay was performed following the same procedures as previously described but with slight modifications<sup>49</sup>. NfMCU proteoliposomes were thawed and sonicated in a bath sonicator for 60 seconds at 15 second intervals before the assay. 100  $\mu\text{L}$  samples were passed through a pre-spun Sephadex G-50 fine gel filtration column (1.5 mL bed volume in a 5 mL disposable spin column) swollen in flux buffer (50 mM HEPES pH 7.4, 150mM KCl or NMDG). The resulting 160  $\mu\text{L}$  of proteoliposome eluent was collected and added to 300  $\mu\text{L}$  of reaction buffer (flux buffer + 0.2 $\mu\text{M}$  valinomycin + 83 $\mu\text{M}$   $^{45}\text{CaCl}_2$ ) to initiate the reaction. At various time points, 75  $\mu\text{L}$  of this reaction mixture was passed through a pre-spun Sephadex G-50 fine gel filtration column as previously described to remove extra-liposomal  $^{45}\text{Ca}$  and stop the flux. The eluent was mixed with 10 mL scintillation cocktail and its radioactivity was measured in a scintillation counter.

For the Ru360 inhibition experiments, NfMCU proteoliposomes in flux buffer (50 mM HEPES pH 7.4, 150mM NMDG) were mixed with reaction buffer containing varying concentrations of Ru360 (dissolved in NMDG flux buffer + 0.2 $\mu$ M valinomycin + 83 $\mu$ M <sup>45</sup>CaCl<sub>2</sub>). The reaction was allowed to proceed for 30 minutes, after which the reaction was stopped by passing 75 $\mu$ L of the reaction through a pre-spun Sephadex G-50 fine gel filtration column as previously described. To determine the relative calcium uptake by NfMCU proteoliposomes, the scintillation count for each sample was normalized to the sample without any Ru360 in the reaction.

**Data availability**

The cryo-EM density maps of the NfMCU have been deposited in the Electron Microscopy Data Bank under accession numbers EMD-7826 (without saposin) and EMD-7828 (with saposin, low-pass filter to 5.0 Å resolution). Atomic coordinates have been deposited in the Protein Data Bank under accession numbers 6D7W (without saposin) and 6D80 (with saposin modeled as poly-A peptide). Source data for Fig. 4e, Fig 5b–d, Extended Data Fig. 1b and Extended Data Fig. 2 are available in Supplementary Information. The gel source data for Fig. 4e, Extended Data Fig. 1b and 1c, and Extended Data Fig. 8 are available in Supplementary Figure 1.

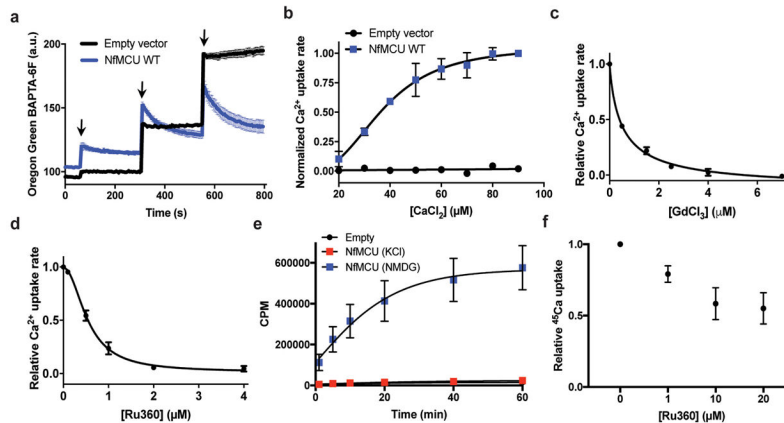
**Extended Data**



**Extended Data Figure 1. Biochemical analysis of NfMCU**

**a**, Representative gel filtration profile of full-length (black trace) versus truncated NfMCU used for cryo-EM studies (blue trace). **b**, Functional activity of full-length (FL) and truncated NfMCU (EM); data shown represent mean  $\pm$  SEM (n=3 independent experiments). Cell lysates were analyzed by immunoblotting using anti-His antibody to detect expression of NfMCU; RpoA was used as loading control. **c**, Detergent solubilized NfMCU (control) separates as a single band at ~46 kDa on Coomassie stained SDS-PAGE and crosslinks as tetramers when treated with chemical crosslinkers of varying spacer arm length. (DSG:

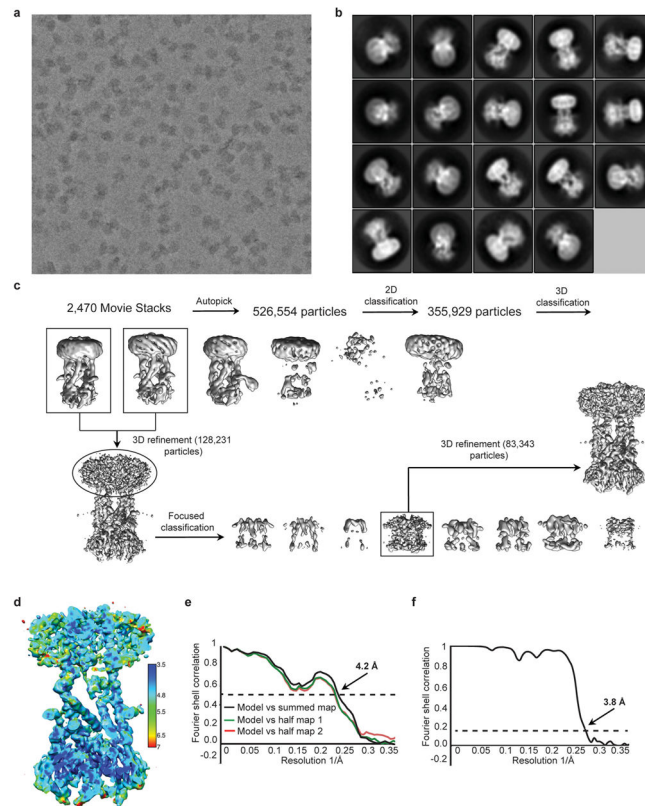
disuccinimidyl glutarate, DSS: disuccinimidyl suberate, BS<sub>3</sub>: bis(sulfosuccinimidyl) suberate, BSPEG<sub>5</sub>: PEGylated bis(sulfosuccinimidyl)suberate). See Supplementary Figure 1 for gel source data. The experiments shown in **a** and **b** were repeated at least three times independently with similar results. The crosslinking experiment shown in **c** was performed once.



**Extended Data Figure 2. Functional characterization of NfMCU**

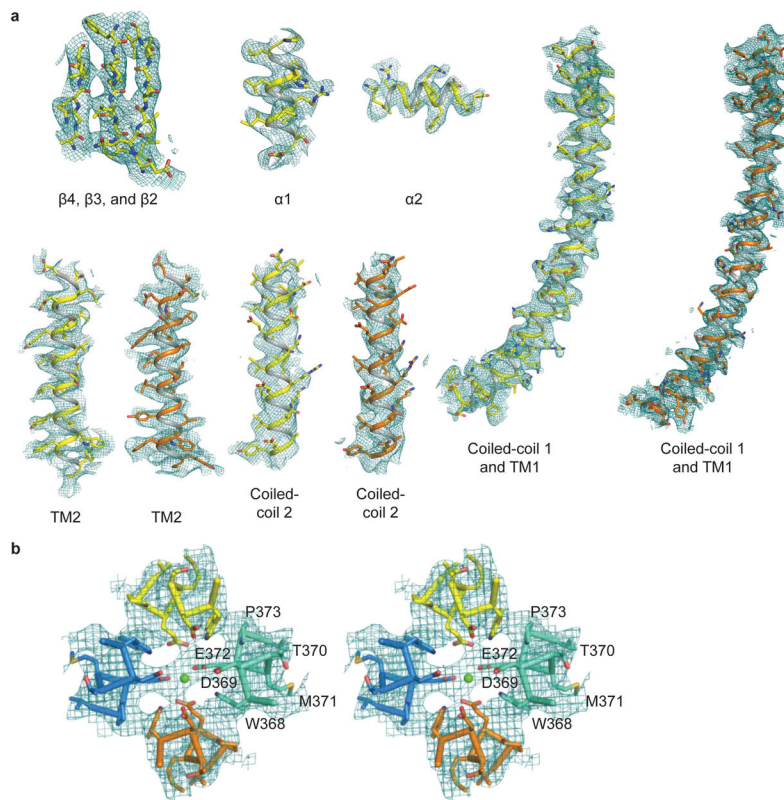
**a**, Calcium uptake in *E. coli* expressing empty vector (black trace) or NfMCU (blue trace), demonstrating that the heterologously expressed NfMCU can confer uniporter function to bacteria. Arrows indicate addition of 20μM CaCl<sub>2</sub> to the reaction solution. **b**, Concentration dependent calcium uptake in *E. coli* expressing empty vector (black trace) or NfMCU (blue trace). Each point represents the rate of calcium uptake normalized to the uptake rate at 90μM CaCl<sub>2</sub>. **c**, Concentration dependent inhibition of NfMCU by GdCl<sub>3</sub> in *E. coli* expressing NfMCU. Each point represents the rate of calcium uptake normalized to the uptake rate without GdCl<sub>3</sub> in the reaction. **d**, Concentration dependent inhibition of Ca<sup>2+</sup> uptake in *E. coli* expressing NfMCU by the MCU-specific inhibitor Ru360. Each point represents the rate of calcium uptake normalized to the uptake rate without Ru360 in the reaction. The Ru360 concentration required to reduce the Ca<sup>2+</sup> uptake rate by half (or IC<sub>50</sub>) is calculated to be 0.5μM. **e**, In light of the contradiction of the oligomeric state between NfMCU and cMCU- NTD, we also designed an *in vitro* functional assay by reconstituting our purified tetrameric channel into liposomes. Unable to obtain currents of NfMCU by electrophysiology – probably due to the channel’s small conductance – we performed a radioactive <sup>45</sup>Ca flux assay on proteoliposomes loaded with 150 mM KCl. Shown here is the time-dependent <sup>45</sup>Ca<sup>2+</sup> uptake by empty liposomes or NfMCU proteoliposomes incubated with <sup>45</sup>Ca<sup>2+</sup> in a reaction buffer containing 150mM KCl (red points) or 150mM NMDG (blue points). The result demonstrates that in a reaction solution containing 150mM NMDG and the K<sup>+</sup>-selective ionophore valinomycin (to generate an electrical driving force), NfMCU proteoliposomes exhibited time-dependent <sup>45</sup>Ca uptake while the same proteoliposomes in a reaction solution containing valinomycin and 150mM KCl (to eliminate electrical driving force) accumulated <sup>45</sup>Ca<sup>2+</sup> only slightly better than empty liposomes, recapitulating the voltage-dependent Ca<sup>2+</sup> uptake property of the MCU. **f**, Concentration dependent inhibition of NfMCU proteoliposomes by Ru360, demonstrating that Ru360 also blocks NfMCU <sup>45</sup>Ca<sup>2+</sup> uptake in a concentration-dependent manner up to

50%, which is expected given an equal distribution of two channel orientations in the liposomes. Each point represents radioactivity measured following 30 min reaction normalized to sample without Ru360. All data points shown in **a–f** are mean  $\pm$  SEM (n=3 independent experiments).



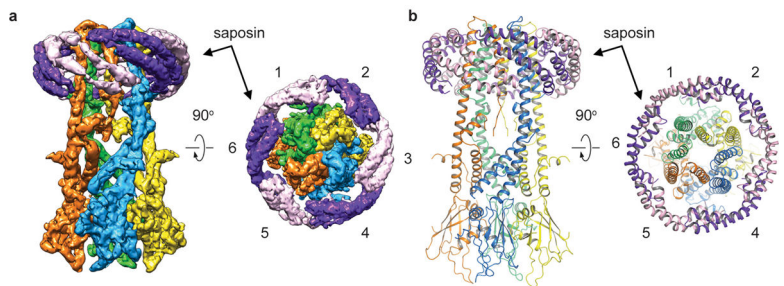
**Extended Data Figure 3. Cryo-EM analysis of NfMCU**

**a**, Representative phase-plate electron micrograph of the NfMCU saposin complex and 2470 micrographs were used for structure determination. **b**, Representative 2D class averages of the NfMCU saposin complex. **c**, Flowchart of data processing to obtain the 3.8 Å cryo-EM map of the NfMCU saposin complex. Details can be found in the “Image processing” section of the Methods. **d**, Local resolution of NfMCU estimated with RELION2.0. **e**, FSC curves for the refined model versus the summed 3.8 Å map (black curve), the refined model versus half map 1 (red curve), and the refined model versus half map 2 that was not used for refinement (green curve). **f**, The gold-standard Fourier shell correlation curve for the cryo-EM map.



**Extended Data Figure 4. EM map of NfMCU**

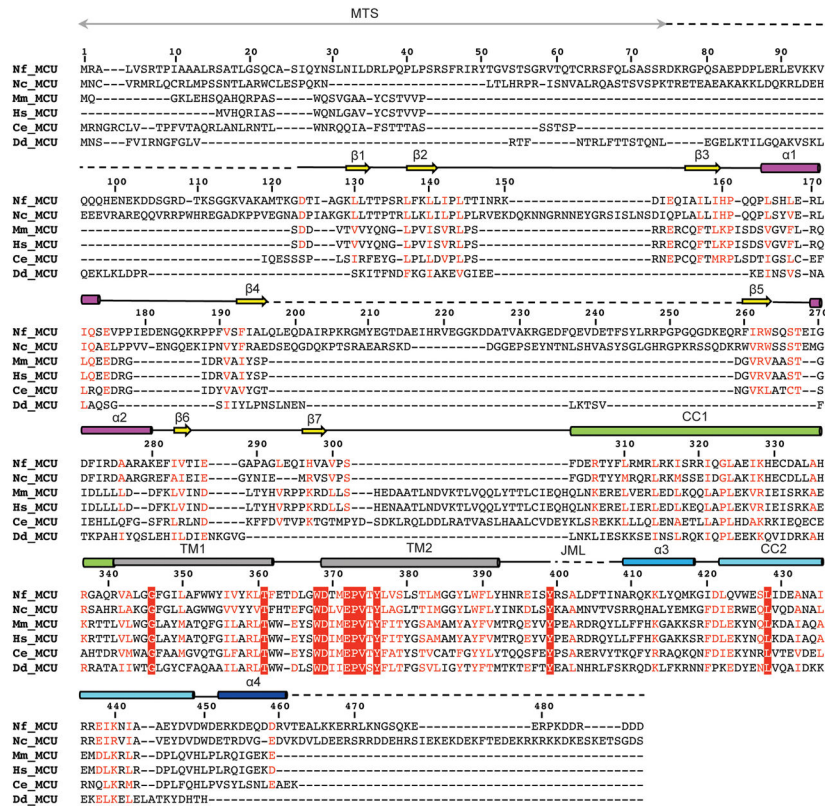
**a**, Representative regions of the EM map of NfMCU highlighting key structural features at the NTD (α1, α2, β2–β3), the coiled-coil domain, and transmembrane domain (TM1 and TM2). Protomer 1 and 2 are shown in yellow and orange, respectively. **b**, Stereo view of the EM map carved around the TM2 filter region of NfMCU.



**Extended Data Figure 5. Cryo-EM structure of NfMCU in complex with saposin**

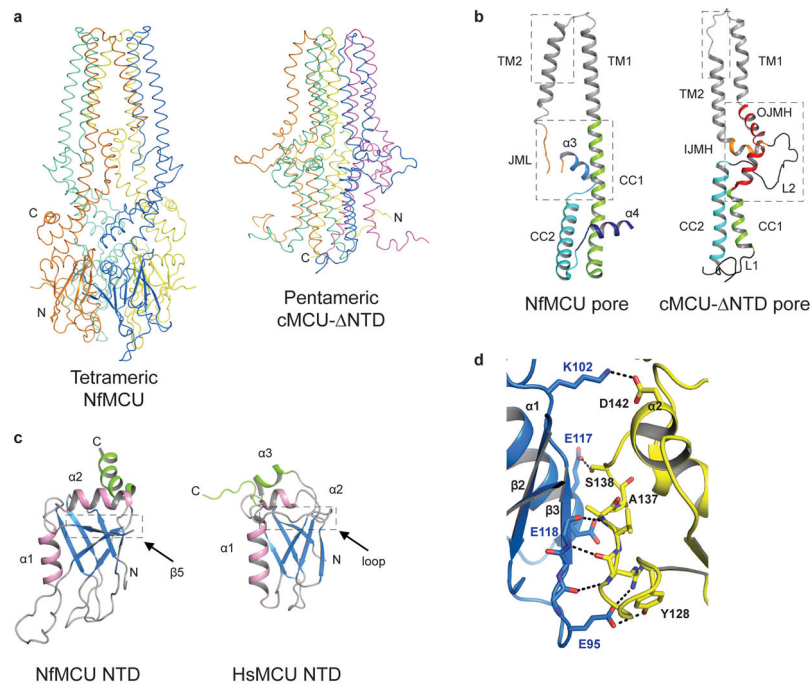
**a**, Cryo-EM map of NfMCU in complex with saposin (shown alternating between purple and pink). The map is low-pass filtered to 5 Å to allow for better visualization of the density from the saposin molecules. Six saposin molecules, each oriented at a 45° angle to the vertical axis, wrap around NfMCU stabilized in lipid. **b**, Ribbon diagram of NfMCU in complex with saposin. Approximately 79–81 residues of the 81-residue saposin molecule was modeled as a poly-alanine chain into the helix-turn-helix EM map density for saposin.





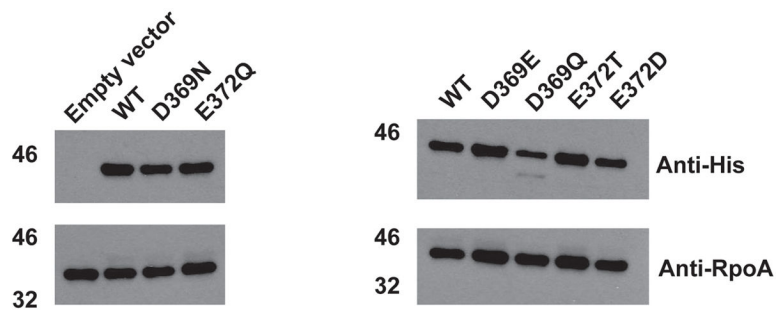
**Extended Data Figure 6. Sequence alignment of MCU orthologs**

The sequences were aligned using PROMALS3D<sup>50</sup> and numbered according to NfMCU. Secondary structures shown above the sequences are based on the cryo-EM structure of NfMCU. Loops are denoted by solid black lines; disordered regions not observed in the cryo-EM structure of NfMCU are indicated by dashed lines; and truncations made to NfMCU at the N- and C-termini are shown as red rectangles. The first 75 residues in NfMCU (colored purple) are predicted to be the mitochondrial targeting sequence (MTS). NCBI accession number for the sequences are: [HsMCU (human MCU): NP\_612366.1, MmMCU (mouse MCU): XP\_006513531.1, DdMCU (*Dictyostelium discoideum* MCU): XP\_637750.1, CeMCU (*C. elegans* MCU): NP\_500892.1, NcMCU (*Neurospora crassa* MCU): XP\_959658.1, NfMCU (*Neosartorya fischeri* MCU): XP\_001266985.1].



**Extended Data Figure 7. Structure comparison between MCU domains**

**a**, Overall structure comparison between tetrameric NfMCU and pentameric cMCU- NTD (PDB: 5ID3). Each subunit is individually colored. **b**, Structure comparison between a single subunit of the pore domain of NfMCU and cMCU- NTD. Dashed boxes indicate major differences between the two structures. Structural features in cMCU- NTD are labeled as in the original structure<sup>16</sup>. (IJMH: inner juxtamembrane helix, OJMH: outer juxtamembrane helix, L1: loop 1, L2: loop 2, JML: juxtamembrane loop, CC1: coiled-coil 1, CC2: coiled coil 2). **c**, Structure comparison between the NTD of NfMCU and HsMCU (PDB: 4XTB). Dashed box indicates the major difference between the two structures. **d**, Atomic interactions between two NTD subunits in the crystal structure of HsMCU NTD, equivalent to interface I identified in the cryo-EM structure of NfMCU.



**Extended Data Figure 8. Western blot analysis of NfMCU expression in *E. coli***

NfMCU, with its mitochondrial targeting sequence removed and replaced with a 6x-His tag, was expressed in *E. coli* for functional analysis. Mouse anti-His antibodies (Qiagen) was used to detect NfMCU expression and mouse anti-RpoA targeting *E. coli* RNA polymerase alpha (Santa Cruz Biotechnology) was used for loading control. See Supplementary Figure 1

for gel source data. The experiment was repeated three times independently with similar results.

### Extended Data Table 1

Cryo-EM data collection and model statistics

	NfMCU (EMDB-7826) (PDB 6D7W)	NfMCU saposin complex (EMDB-7828) (PDB 6D80)
<b>Data collection and processing</b>		
Magnification	59,523	59,523
Voltage (kV)	300	300
Electron exposure (e-/Å <sup>2</sup> )	60	60
Defocus range (μm)	-0.5	-0.5
Pixel size (Å)	0.84	0.84
Symmetry imposed	C2	C2
Initial particle images (no.)	526,554	526,554
Final particle images (no.)	128,231	128,231
Map resolution (Å)	3.8	5.0
FSC threshold	0.143	0.143
Map resolution range (Å)	184.8-3.8	184.8-5.0
<b>Refinement</b>		
Initial model used (PDB code)	Initial model generated in RELION2.0	Initial model generated in RELION2.0
Model resolution (Å)	3.8	5.0
FSC threshold	0.143	0.143
Model resolution range (Å)	184.8-3.8	184.8-5.0
Map sharpening <i>B</i> factor (Å <sup>2</sup> )	-120	-120
Model composition		
Non-hydrogen atoms	8,946	11,351
Protein residues	1,087	1,568
Ligands	1	
<i>B</i> factors (Å <sup>2</sup> )	103.55	135.43
Protein	103.55	135.43
Ligand	127.22	127.22
R.m.s. deviations		
Bond lengths (Å)	0.008	0.007
Bond angles (°)	1.396	1.306
Validation		
MolProbity score	2.41	2.33
Clashscore	14	13
Poor rotamers (%)	0.9	0.9
Ramachandran plot		
Favored (%)	93	93
Allowed (%)	7	7
Disallowed (%)	0	0

## Supplementary Material

Refer to Web version on PubMed Central for supplementary material.

## Acknowledgments

We thank J. Guo and Q. Chen for technical assistance and manuscript preparation and J. Frauenfeld (Salipro Biotech) for the recombinant saposin construct. Negative stained EM data and sample optimization for cryo-EM was performed at the University of California San Francisco; we thank M. Braunfeld for supervision of the microscopes. Phase plate cryo-EM data were collected at the University of Texas Southwestern Medical Center Cryo-EM Facility that is funded by the CPRIT Core Facility Support Award RP170644; we thank D. Nicastro and Z. Chen for technical support and facility access. This work was supported in part by the Howard Hughes Medical Institute (to Y.J., V.K.M. and Y.C.), the National Institutes of Health (grant GM079179 to Y.J.; grants R01GM098672, S10OD020054, and S10OD021741 to Y.C.), the Welch Foundation (Grant I-1578 to Y.J.), the Cancer Prevention and Research Initiative of Texas (to X.B.) and the Virginia Murchison Linthicum Scholar in Medical Research fund (to X.B.).

## References

1. Kamer KJ, Mootha VK. The molecular era of the mitochondrial calcium uniporter. *Nat Rev Mol Cell Biol.* 2015; 16:545–553. [PubMed: 26285678]
2. Berridge MJ, Bootman MD, Roderick HL. Calcium signaling: dynamics, homeostasis and remodeling. *Nat Rev Mol Cell Biol.* 2003; 4:517–529. [PubMed: 12838335]
3. Kirichok Y, Krapivinsky G, Clapham DE. The mitochondrial calcium is a highly selective ion channel. *Nature.* 2004; 427:360–364. [PubMed: 14737170]
4. Baughman JM, Perocchi F, Girgis H, Plovanich M, Belcher-Timme CA, Sancak Y, Bao XR, Strittmatter L, Goldberger O, Bogorad RL, et al. Integrative genomics identifies MCU as an essential component of the mitochondrial calcium uniporter. *Nature.* 2011; 476:341–345. [PubMed: 21685886]
5. De Stefani D, Raffaello A, Teardo E, Szabo I, Rizzuto R. A forty-kilodalton protein of the inner membrane is the mitochondrial calcium uniporter. *Nature.* 2011; 476:336–340. [PubMed: 21685888]
6. Sancak Y, Markhard A, Kitami T, Kovacs-Bogdan E, Kamer KJ, Udeshi ND, Carr SA, Chaudhuri D, Clapham DE, Li AA, Calvo SE, Goldberger O, Mootha VK. EMRE is an essential component of the mitochondrial calcium uniporter. *Science.* 2013; 342:1379–1382. [PubMed: 24231807]
7. Plovanich M, Bogorad RL, Sancak Y, Kamer KJ, Strittmatter L, Li AA, Girgis HS, Kuchimanchi S, De Groot J, Speciner L, et al. MICU2, a paralog of MICU1, resides within the mitochondrial uniporter complex to regulate calcium handling. *PLoS One.* 2013; 8:e55785. [PubMed: 23409044]
8. Perocchi F, Gohil VM, Girgis HS, Bao XR, McCombs JE, Palmer AE, Mootha VK. MICU1 encodes a mitochondrial EF hand protein required for Ca(2+) uptake. *Nature.* 2010; 467:291–296. [PubMed: 20693986]
9. Tsai M-F, Phillips CB, Ranaghan M, Tsai C-W, Wu Y, Williams C, Miller C. Dual functions of a small regulatory subunit in the mitochondrial calcium uniporter complex. *eLife.* 2016:e15545. [PubMed: 27099988]
10. Kovacs-Bogdan E, Sancak Y, Kamer KJ, Plovanich M, Jambhekar A, Huber RJ, Myre MA, Blower MD, Mootha VK. Reconstitution of the mitochondrial calcium uniporter in yeast. *Proc Natl Acad Sci USA.* 2014; 111:8985–8990. [PubMed: 24889638]
11. Carafoli E, Lehninger AL. A survey of the interaction of calcium ions with mitochondria from different tissues and species. *Biochem J.* 1971; 122:681–690. [PubMed: 5129264]
12. Bick AG, Calvo SE, Mootha VK. Evolutionary diversity of the mitochondrial calcium uniporter. *Science.* 2012; 336:886. [PubMed: 22605770]
13. Song J, Liu X, Zhai P, Huang J, Lu L. A putative mitochondrial calcium uniporter in *A. fumigatus* contributes to mitochondrial Ca<sup>2+</sup> homeostasis and stress responses. *Fungal Genet Biol.* 2016; 94:15–22. [PubMed: 27378202]

14. Lee Y, Min CK, Kim TG, Song HK, Lim Y, Kim D, Shin K, Kang M, Kang JY, Youn HS, et al. Structure and function of the N-terminal domain of the human mitochondrial calcium uniporter. *EMBO Rep.* 2015; 16:1318–1333. [PubMed: 26341627]
15. Kishnani PS, et al. Immune response to enzyme replacement therapies in lysosomal storage diseases and the role of immune tolerance induction. *Mol Genet Metab.* 2016; 117:66–83. DOI: 10.1016/j.ymgme.2015.11.001 [PubMed: 26597321]
16. Oxenoid KDY, Cao C, Cui T, Sancak Y, Markhard A, Grabarek Z, Kong L, Liu Z, Ouyang B, et al. Architecture of the mitochondrial calcium uniporter. *Nature.* 2016; 533:269–273. [PubMed: 27135929]
17. Wang L, Yang X, Li S, Wang Z, Liu Y, Feng J, Zhu Y, Shen Y. Structural and mechanistic insights into MICU1 regulation of mitochondrial calcium uptake. *EMBO J.* 2014; 33:594–604. [PubMed: 24514027]
18. Logan CV, Szabadkai G, Sharpe JA, Parry DA, Torelli S, Childs AM, Kriek M, Phadke R, Johnson CA, Roberts NY, et al. Loss of function mutations in MICU1 cause a brain and muscle disorder linked to primary alterations in mitochondrial calcium signaling. *Nat Genet.* 2014; 46:188–193. [PubMed: 24336167]
19. Gunter TE, Pfeiffer DR. Mechanisms by which mitochondria transport calcium. *Am J Physiol.* 1990; 258:C755–786. [PubMed: 2185657]
20. Frauenfeld J, Loving R, Armache JP, Sonnen AFP, Guettou F, Moberg P, Zhu L, Jegerschold C, Flayhan A, Briggs JAG, Garoff H, Low C, Cheng Y, Nordlund P. A saposin-lipoprotein nanoparticle system for membrane proteins. *Nat Methods.* 2016; 13:345–351. [PubMed: 26950744]
21. Doyle DA, Morais Cabral J, Pfuetzner RA, Kuo A, Gulbis JM, Cohen SL, Chait BT, MacKinnon R. The structure of the potassium channel: molecular basis of K<sup>+</sup> conduction and selectivity. *Science.* 1998; 280:69–77. [PubMed: 9525859]
22. Biedermannova L, Riley KE, Berka K, Hobza P, Vondrasek J. Another role of proline: stabilization interactions in proteins and protein complexes concerning proline and tryptophane. *Phys Chem Chem Phys.* 2008; 10:6350–6359. [PubMed: 18972023]
23. Zondlo NJ. Aromatic-proline interactions: electronically tunable CH/interactions. *Acc Chem Res.* 2013; 46:1039–1049. [PubMed: 23148796]
24. Mallilankaraman K, Doonan P, Cardenas C, Chandramoorthy HC, Muller M, Miller R, Hoffman NE, Gandhirajan RK, Molgo J, Birnbaum MJ, et al. MICU1 is an essential gatekeeper for MCU-mediated mitochondrial Ca<sup>2+</sup> uptake that regulates cell survival. *Cell.* 2012; 151:630–644. [PubMed: 23101630]
25. Kamer KJ, Mootha VK. MICU1 and MICU2 play nonredundant roles in the regulation of the mitochondrial calcium uniporter. *EMBO Rep.* 2014; 15:299–307. [PubMed: 24503055]
26. Patron M, Checchetto V, Raffaello A, Teardo E, Reane DV, Mantoan M, Granatiero V, Szabo I, De Stefani D, Rizzuto R. MICU1 and MICU2 finely tune the mitochondrial Ca<sup>2+</sup> uniporter by exerting opposite effects on MCU activity. *Mol Cell.* 2014; 53:726–737. [PubMed: 24560927]
27. Liu JC, Liu J, Holmstrom KM, Menazza S, Parks RJ, Fergusson MM, Yu ZX, Springer DA, Halsey C, Liu C, et al. MICU1 serves as a molecular gatekeeper to prevent in vivo mitochondrial calcium overload. *Cell Rep.* 2016; 16:1561–1573. [PubMed: 27477272]
28. Almers W, McCleskey EW. Non-selective conductance in calcium channels of frog muscle: calcium selectivity in a single-file pore. *J Physiol.* 1984; 353
29. Hess P, Tsien RW. Mechanism of ion permeation through calcium channels. *Nature.* 1984; 301:453–456.
30. Heinemann SH, Terlau H, Stühmer W, Imoto K, Numa S. Calcium channel characteristics conferred on the sodium channel by single mutations. *Nature.* 1992; 356:441–443. [PubMed: 1313551]
31. Cao C, Wang S, Cui T, Su XC, Chou JJ. Ion and inhibitor binding of the double-ring ion selectivity filter of the mitochondrial calcium uniporter. *Proc Natl Acad Sci USA.* 2017; 114:E2846–E2851. [PubMed: 28325874]
32. Pei J, Kim BH, Grishin NV. PROMALS3D: a tool for multiple protein sequence and structure alignments. *Nucleic Acids Res.* 2008; 36:2295–2300. [PubMed: 18287115]

33. Qing G, Ma L, Khorchid K, Swapna GVT, Mal TK, Takayama MM, Xia B, Phadtare S, Ke H, Acton T, Montelione GT, Ikura M, Inouye M. Cold-shock induced high-yield protein production in *Escherichia coli*. *Nat Biotechnol*. 2004; 22:877–882. [PubMed: 15195104]
34. Danev R, Tegunov D, Baumeister W. Using the Volta phase plate with defocus for cryo-EM single particle analysis. *eLife*. 2017; 6:e23006. [PubMed: 28109158]
35. Zheng SQ, Palovcak E, Armache JP, Verba KA, Cheng Y, Agard DA. MotionCor2: anisotropic correction of beam-induced motion for improved cryo-electron microscopy. *Nat Methods*. 2017; 14:331–332. [PubMed: 28250466]
36. Zhang K. Gctf: Real-time CTF determination and correction. *J Struct Biol*. 2016; 193:1–12. [PubMed: 26592709]
37. Scheres SH. RELION: implementation of a Bayesian approach to cryo-EM structure determination. *J Struct Biol*. 2012; 180:519–530. [PubMed: 23000701]
38. Bai XC, Rajendra E, Yang G, Shi Y, Scheres SH. Sampling the conformational space of the catalytic subunit of human gamma-secretase. *eLife*. 2015; 4:e11182. [PubMed: 26623517]
39. Kucukelbir A, Sigworth FJ, Tagare HD. Quantifying the local resolution of cryo-EM density maps. *Nat Methods*. 2014; 11:63–65. [PubMed: 24213166]
40. Emsley P, Lohkamp B, Scott WG, Cowtan K. Features and development of Coot. *Acta Crystallographica D*. 2010; 66:486–501.
41. Adams PD, et al. PHENIX: a comprehensive Python-based system for macromolecular structure solution. *Acta Crystallographica D*. 2010; 66:213–221.
42. Amunts A, et al. Structure of the yeast mitochondrial large ribosomal subunit. *Science*. 2014; 343:1485–1489. [PubMed: 24675956]
43. DiMaio F, Zhang J, Chiu W, Baker D. Cryo-EM model validation using independent map reconstructions. *Protein Sci*. 2013; 22:865–868. [PubMed: 23592445]
44. Chen VB, Arendall WB 3rd, Headd JJ, Keedy DA, Immormino RM, Kapral GJ, Murray LW, Richardson JS, Richardson DC. MolProbity: all-atom structure validation for macromolecular crystallography. *Acta Crystallographica D*. 2010; 66:12–21.
45. Smart OS, Neduvélil JG, Wang X, Wallace BA, Sansom MS. HOLE: a program for the analysis of the pore dimensions of ion channel structural models. *J Mol Graph*. 1996; 14:354–360. [PubMed: 9195488]
46. SchrödingerL. The PyMOL Molecular Graphics System, Version 1.8.2015
47. Pettersen EF, Goddard TD, Huang CC, Couch GS, Greenblatt DM, Meng EC, Ferrin TE. UCSF Chimera—a visualization system for exploratory research and analysis. *J Comput Chem*. 2005; 25:1605–1612.
48. Yaffe M. Analysis of mitochondrial function and assembly. *Methods Enzymol*. 1991; 194:627–643. [PubMed: 2005813]
49. Lo CJ, Leake MC, Pilizota T, Berry RM. Nonequivalence of membrane voltage and ion-gradient as driving forces for the bacterial flagellar motor at low load. *Biophys J*. 2007; 93:294–302. [PubMed: 17416615]
50. Heginbotham L, Kolmakova-Partensky L, Miller C. Functional reconstitution of a prokaryotic K<sup>+</sup> channel. *J Gen Physiol*. 1998; 111:741–749. [PubMed: 9607934]

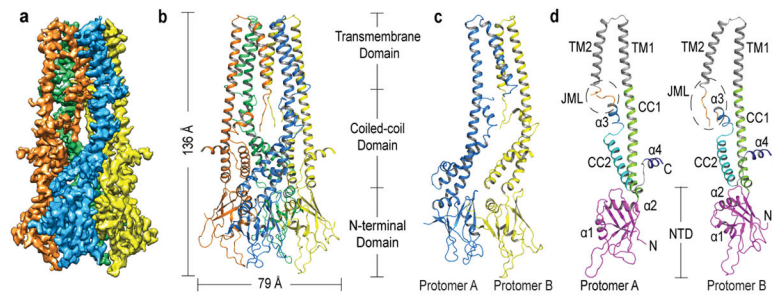


**Figure 1. Cryo-EM structure of NfMCU**  
**a**, The overall cryo-EM map of NfMCU with density for saposin removed for clarity. **b**, Overall architecture of NfMCU colored by subunit and divided into major structural domains. **c**, Each NfMCU tetramer assembles as a dimer of dimer. Each dimer consists of two protomers adopting distinct conformations. **d**, Structural comparison of the two protomers in each MCU dimer. Dashed circles highlight the distinct conformation of the juxtamembrane loop (JML) in the two protomers.

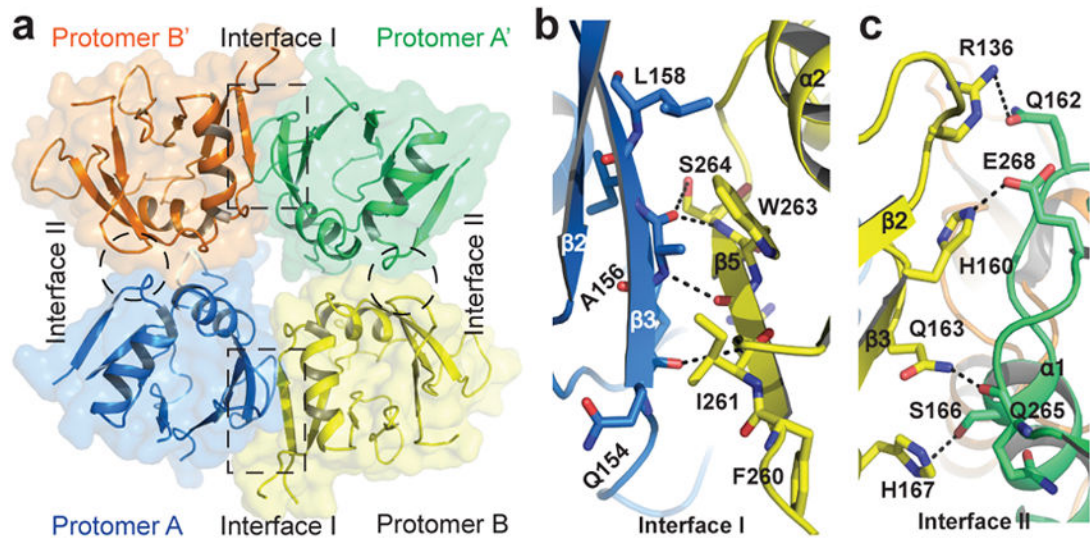


**Figure 2. Channel assembly and subunit interfaces at the NTD**

**a**, Top view of surface rendered NfMCU showing inter-subunit interactions at the NTD. **b**, Detailed view of atomic interactions at interface I in NfMCU consisting of hydrogen bonds mainly between main chain atoms. **c**, Atomic interactions at interface II consist of mainly side chain hydrogen bonds.



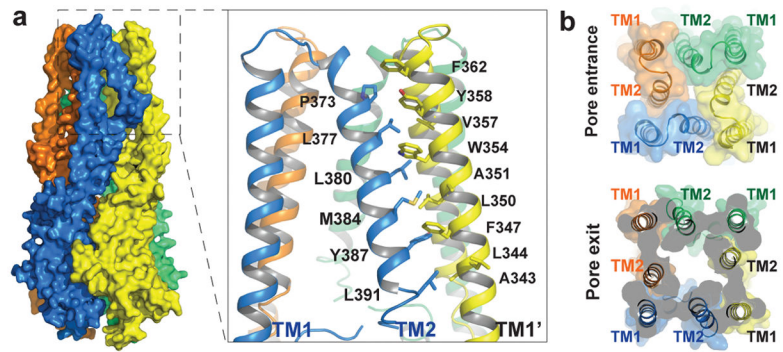


**Figure 3. Channel assembly and subunit interfaces at the TMD**

**a**, Surface rendered model of NfMCU with zoomed-in view of the inter-subunit interactions at the TMD between TM2 of one subunit and TM1 of a neighboring subunit. **b**, Top view of NfMCU at the pore entrance and exit, highlighting the unique arrangement of the TM helices in channel assembly and the widening of the pore moving down the ion conduction pathway.

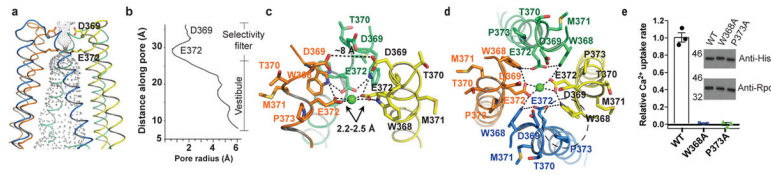


**Figure 4. Ion conduction pore of NfMCU**

**a**, Ribbon diagram of the NfMCU pore domain with the ion conduction pathway rendered as gray mesh and one pair of the acidic filter residues (D369 and E372) shown as sticks. **b**, Pore radius along the central axis. **c**, Side view of the selectivity filter region with the front subunit removed for clarity, highlighting the arrangement of the DIME motif and the approximate cross distance measurements between D369 residues and  $\text{Ca}^{2+}$  coordination distances for E372 (shown as dashed lines). **d**, Top view of the selectivity filter region. E372 forms a hydrogen bond network with W368.  $\text{Ca}^{2+}$  (green sphere) is coordinated by a pair of E372 in a bidentate manner. Dashed circle marks the inter-subunit packing between W368 and P373. **e**, Functional activity of NfMCU W368 and P373 mutants expressed in *E. coli*. Data points are mean  $\pm$  SEM ( $n=3$  independent experiments). Protein expression level was analyzed by immunoblotting using *E. coli* RNA polymerase alpha (RpoA) as control (Methods). The experiment was repeated three times independently with similar results.

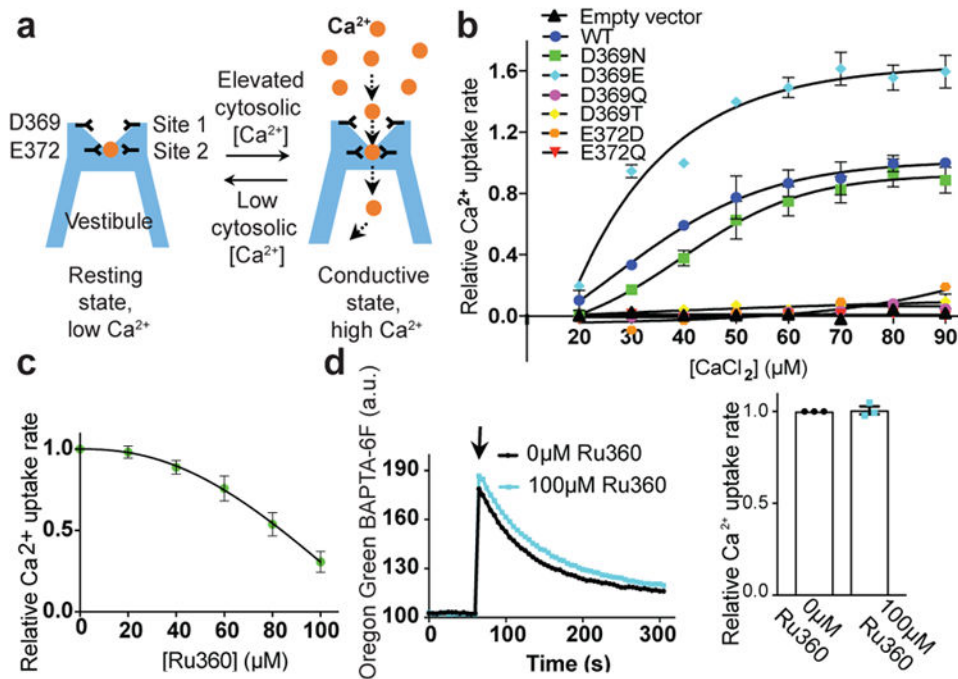


**Figure 5. Mechanism of ion transport and Ru360 inhibition**  
**a**, Proposed model of calcium permeation in NfMCU. **b**, Concentration dependent calcium uptake in *E. coli* expressing NfMCU filter mutations. Data are normalized to the calcium uptake rate of wild-type NfMCU at  $90\mu M$   $CaCl_2$ . **c**, Normalized concentration dependent Ru360 inhibition of *E. coli* expressing NfMCU D369N. **d**, Representative calcium uptake trace for *E. coli* expressing NfMCU D369E mutant with or without Ru360. Arrow indicates addition of  $50\mu M$   $CaCl_2$  to the reaction. Bar graph shows the rate of calcium uptake normalized to the uptake rate without Ru360 in the reaction. All data points shown in **b–c** are mean  $\pm$  SEM ( $n=3$  independent experiments).